

21 **Abstract**

22 Ocean alkalinity enhancement (OAE) is a strategy for marine carbon dioxide removal that aims to increase the
23 total alkalinity (TA) of seawater to sequester atmospheric CO₂ in the form of dissolved inorganic carbon (DIC). An
24 intense alkalization of seawater resulting from OAE treatment could trigger a significant runaway carbonate
25 precipitation process, which may lead to a loss of initially added TA, thereby limiting its efficiency. Even under
26 natural background aragonite saturation states, a continuous yet barely detectable loss of TA is theoretically
27 expected to occur in seawater. With the additional increase through OAE, time ranges to initiate an appreciable
28 TA-loss process could be reduced significantly. Therefore, predicting the TA stability ranges might be a necessity
29 for application scenarios. The main drivers of the precipitation process are i) the aragonite saturation state of
30 seawater and ii) the available surface area for heterogeneous precipitation.

31 In this study, we refined the use of logistic functions to describe the temporal evolution of both drivers, with
32 experimental datasets using natural seawater from the Raunefjorden (Bergen, Norway; Temp.: ~11°C, Sal.:
33 ~32.6). The observed patterns were then used to derive a process-based model for calculating TA-loss rates,
34 focusing on the accelerated precipitation phase of the runaway process while considering saturation levels and
35 available particle surface area. The formation of carbonate phases reduces seawater TA concentrations, inducing
36 a delay or stopping the TA-loss process. In addition, the sinking of precipitated particles decreases the potential
37 for further precipitation by reducing the available surface area in the system. To assess the impact of particle
38 sinking on TA-loss, their shape and size distribution were determined. Under the environmental conditions
39 presented here, TA-loss rates could be reduced by up to 30-40% due to the sinking of particles, after just one
40 day.

41 Integrating the proposed concepts into ocean models could enhance the accuracy of predictions regarding the
42 fate of added TA. Gaining insights into the evolution of the identified, seemingly stable TA levels can help prevent
43 accelerated precipitation phases. Additionally, an understanding of particle sinking or dilution processes reducing
44 the available reactive particle surface area is relevant to assess the efficacy and durability of OAE.

45

46 **1 Introduction**

47 To mitigate climate change and reach net-zero greenhouse gas emissions by the end of the century, negative
48 emission technologies (NETs) are necessary besides greenhouse gas emission reduction (UNFCCC, 2015)
49 considering the slow change in the development of the energy infrastructure, lifestyle of humanity, and national
50 goals for economic growth (Fuss et al., 2018; Iyer et al., 2015; Sers & Victor, 2018). Various carbon dioxide
51 removal (CDR) technologies have been proposed to help achieve the necessary negative emission trajectories
52 (Hartmann et al., 2013; IPCC, 2023; Minx et al., 2018; Rogelj et al., 2018). Among these, ocean alkalinity
53 enhancement (OAE) is a promising CDR method (Harvey, 2008; Ilyina et al., 2013; Kheshgi, 1995; Rau & Caldeira,
54 1999), with the potential to geochemically sequester 3-30 Gt CO₂ yr⁻¹ (Oschlies et al., 2023; Renforth &
55 Henderson, 2017).

56 Enhancing total alkalinity (TA) could be achieved by two addition approaches: **1.** a non-CO₂-equilibrated (neq) or
57 **2.** a CO₂-equilibrated (eq) (Schulz et al., 2023). Through the neq approach, alkaline materials, such as silicate or
58 hydroxide-based mineral phases could be introduced to seawater in the form of solids or solutions, allowing
59 longer-term CO₂ equilibration with the atmosphere through ingassing of atmospheric CO₂. In the eq approach,
60 already partially pre-CO₂-equilibrated solutions or carbonate-based substances could be released into seawater.
61 Neq TA addition strategies induce greater variations in the affected carbonate system, resulting in drastically
62 reduced *p*CO₂ and a rapid increase in pH values. While an eq TA addition results in less severe changes in ocean
63 chemistry, it is less efficient in generating carbon sequestration potential (Schulz et al., 2023; Suitner et al., 2024).
64 Depending on the introduced alkalinization method (see Eisaman et al., 2023) and the magnitude of treatment,
65 induced changes in the carbonate system could lead to adverse effects on biota (Faucher et al., 2024; Ferderer
66 et al., 2022; Gately et al., 2023; Goldenberg et al., 2024; Marín-Samper et al., 2024; Sánchez et al., 2024; Xin et
67 al., 2024) or in case of persistent oversaturation, result in the precipitation of secondary mineral phases and
68 therefore a loss of the introduced TA (Ilyina et al., 2013; Schulz et al., 2023). The process of TA leakage as a
69 consequence of OAE was recently described by several studies (see Fuhr et al., 2022; Hartmann et al., 2023;
70 Moras et al., 2022; Pan et al., 2021; Ringham et al., 2024; Suitner et al., 2024; Varliero et al., 2024). Within these
71 laboratory-based studies, self-sustaining runaway carbonate precipitation processes led to a significant decrease
72 in the added TA, which could even result in a net-loss of TA. TA stability ranges, and the evolution of the
73 precipitation process depend on the specific local environmental conditions such as temperature, salinity,
74 aragonite saturation state (Ω_{ar}), or suspended particle load of the treated water mass (Moras et al., 2024).

75 The objective of this study is to demonstrate the general capability to predict and parametrize the temporal
76 evolution of a triggered runaway carbonate precipitation process during OAE approaches, based on quantifiable
77 and measurable parameters. Estimations of stability ranges for the permanence of introduced TA additions were
78 derived from these parametrizations. The ability to predict TA stability ranges can help prevent secondary
79 mineral formation and optimize assessments for future OAE application scenarios.

80 Suitner et al. (2024) demonstrated the potential of utilizing inverse logistic functions to depict the temporal
81 evolution of the TA-loss process during the runaway carbonate formation phase (see Fig. 1). In this study,
82 principal descriptive parameters such as TA addition and stability ranges to trigger the runaway process or the

83 timespan of the precipitation phase could be formalized based on their experimental dataset. This approach also
 84 offers the possibility of a straightforward integration of time-dependent loss terms into predictive computational
 85 models simulating OAE addition scenarios, as presented by He & Tyka (2023), Ou et al. (2025), Schwinger et al.
 86 (2024) or Zhou et al. (2024).

87 The application of OAE may exceed critical levels for carbonate precipitation. For open ocean scenarios the rapid
 88 initiation of mixing processes would efficiently reduce the potential for secondary carbonate formation.
 89 Nevertheless, runaway carbonate formation may occur within enclosed geographic locations with physical
 90 features such as bays, estuaries, or lagoons. In addition, thermohaline layering (Bialik et al., 2022) or high
 91 sediment load (Wurgaft et al., 2016, 2021) might create conditions that lead to TA-loss processes.

92 To sustain a triggered runaway carbonate formation (Fig. 1), it is necessary to retain the precipitates in the
 93 system. Removal of these particles reduces the potential for continuous heterogeneous precipitation, thereby
 94 slowing down or halting the process. In this study, the empirically determined TA-loss rates were used to derive
 95 the quantity of precipitated particles. By identifying the particle sizes, shapes, densities, and sinking velocities,
 96 their potential residence times in the water column were estimated. Furthermore, we evaluated whether the
 97 formation of secondary minerals can supply sufficient surface area for a continuous detectable heterogeneous
 98 runaway process in an open-water body and whether the process would be interrupted or attenuated by
 99 removing particles due to their descent into deeper layers.

100

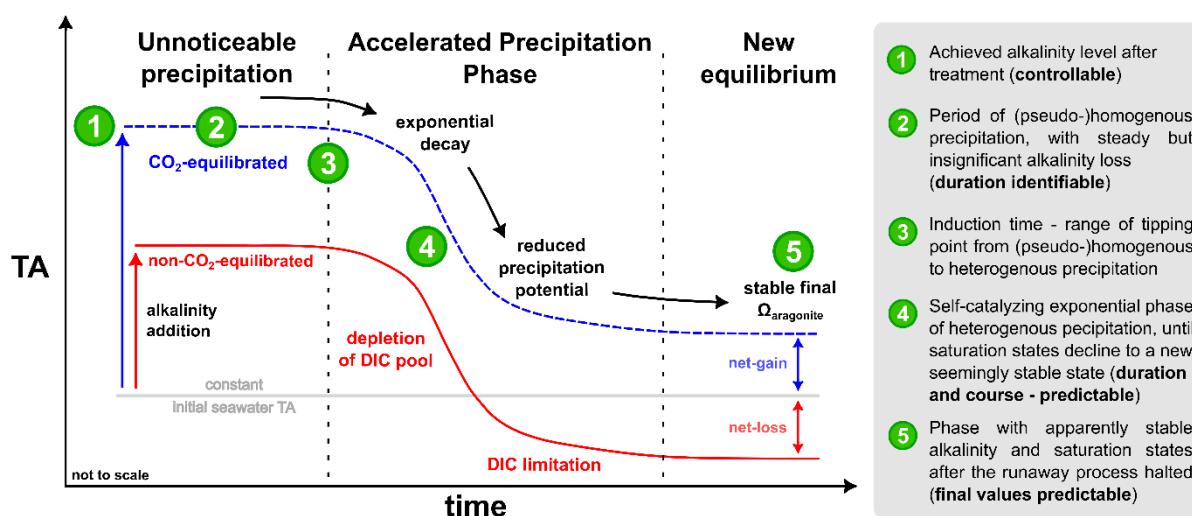


Figure 1: Modified conceptual scheme of a runaway carbonate precipitation process following liquid TA addition after Fig. 9 in Suitner et al., 2024 (not to scale).

101

102 2 Material and methods

103 2.1 Overview of experimental setups

104 Three incubation experiments were conducted to examine the stability of TA of the local “filtered” (mesh size
105 0.2 μm) and “unfiltered” (mesh size 50 μm) seawater of the Raunefjorden, Norway (60.27° N, 5.20° E). Within
106 TA-gradient approaches, 250 ml polystyrene cell culture bottles were filled with natural seawater and incubated
107 in a flow-through incubation box, following the natural light and temperature conditions. Runaway precipitation
108 was observed in eq and neq treatments, after surpassing specific time and TA addition ranges, allowing the
109 description of patterns during the precipitation process. A detailed description of the experimental results,
110 design and methods is given in Suitner et al. (2024), a brief overview is also provided in Tab. 1 (also see SI for
111 further details).

112

Table 1: Overview of the experimental design of precipitation experiments.

#	filter mesh size	CO ₂ state to atmosphere	Alkaline material	Runtime [days]	Range TA _{added} [$\mu\text{mol kg}^{-1}$]	TA _{added} gradient steps [$\mu\text{mol kg}^{-1}$]	Temperature [°C]
I	50 μm	non-equilibrated (neq)	NaOH	25	0-2800	200	10-11
II	0.2 μm				0-3400		11-13
III	0.2 μm	air-equilibrated (eq)	Na ₂ CO ₃ / NaHCO ₃	20	0-9200	800	12-16

113

114 2.2 Curve fitting of the TA and Ω_{ar} evolution

115 The numerical curve fit model to describe the temporal development of TA and Ω_{ar} , as presented in Suitner et al.
116 (2024), was refined by additionally including the observed TA-loss rates as a second input factor, to provide
117 continuous functions as a basis for further model calculations. The curve fit model utilized the consistent
118 tendency of all observed runaway precipitation processes to follow inverse logistic trends in form of:

$$119 \quad f(t) = a e^{-b e^{-ct}} + d \quad (1)$$

120 for the temporal evolution of TA and Ω_{ar} . The coefficients **(d)** and **(a)** are defined by the achieved level of TA/ Ω_{ar}
121 after the addition **(d)** and the final reached value after the runaway process halted **(a)**. Since these factors are
122 predefined by the experimental setup, the curve fit model only numerically parameterizes the two coefficients
123 **(b)** and **(c)**. Coefficient **(b)** represents the “induction time”, or the time required for CaCO₃ precipitation to
124 become detectable in the TA measurements, depicted by the horizontal translation along the x-axis, while **(c)**
125 denotes the timespan between start and end of an accelerated precipitation phase (APP). See Fig. 2 for a visual
126 impression of the influence of iterations of each coefficient.

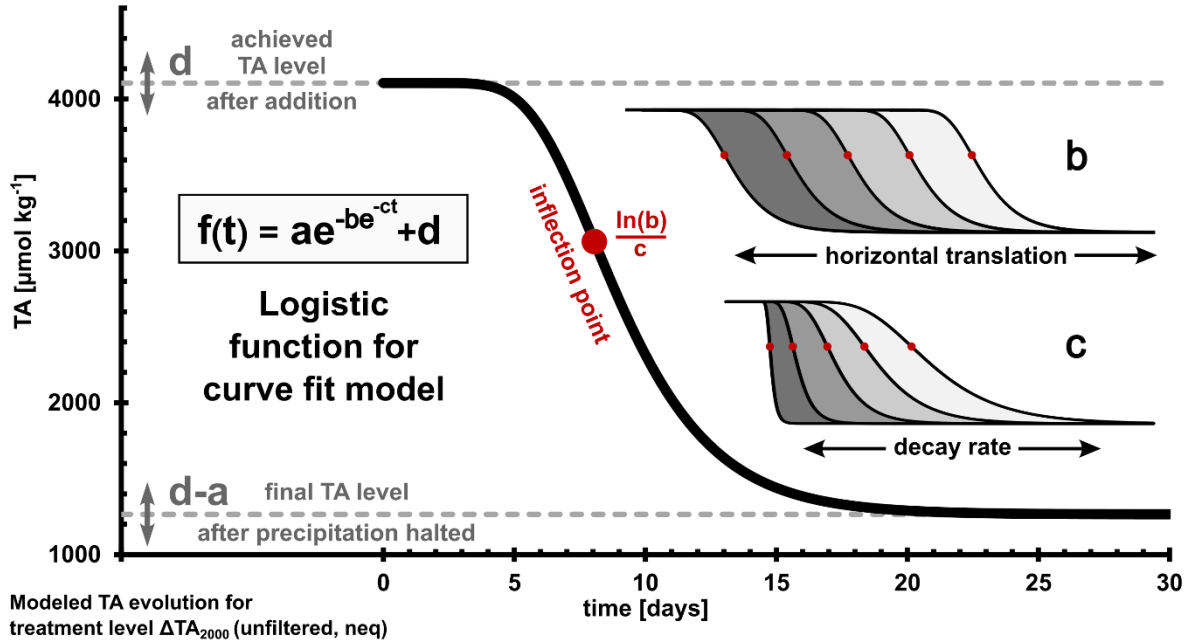


Figure 2: Overview and iterations of each coefficient (a)-(d) of the applied inverse logistic function for the numerical curve fitting; the inflection point is defined by $\ln(b)/c$; for further characteristics see Tjørve & Tjørve (2017).

127

128 2.3 Empirical rate law and determination of loss rates

129 A simple empirical rate law was used to evaluate the precipitation rates R [$\mu\text{mol m}^{-2} \text{h}^{-1}$] (see e.g. Inskeep &
130 Bloom, 1985; Morse et al., 2007; Zhong & Mucci, 1989):

$$131 \quad R = k(\Omega_{ar} - 1)^n \quad (2)$$

132 The experimental TA-loss rates were then fitted to the logarithmic form of Eq. (2) to determine the coefficients
133 k (rate constant) and n (empirical reaction order):

$$134 \quad \log(R) = n(\Omega_{ar} - 1) + \log(k) \quad (3)$$

135 To correct for the variable surface area, r [$\mu\text{mol h}^{-1}$] was normalized for the assumed available active mineral
136 surface area (A in [m^2]) (adapted from Sjöberg, 1976).

$$137 \quad r = k A (\Omega_{ar} - 1)^n \quad (4)$$

138 As the gradient approaches could not provide a sufficient amount of precipitates to determine their surface area,
139 a one-week side experiment was conducted to estimate the mineral surface area generated during the runaway
140 precipitation process. By adding 3.8 mmol NaOH and 7.0 mmol NaHCO_3 to 40 L of 0.2 μm filtered natural
141 seawater (salinity 33) at 23°C, around 5 g of aragonite precipitates were generated to provide material for a BET
142 surface area measurement. Using N_2 adsorption (Brunauer et al., 1938), with a Quantachrome autosorb iQ at the
143 University of Hamburg, a surface area of $2.283 \pm 0.018 \text{ m}^2 \text{ g}^{-1}$ was determined. By the assumption that the surface
144 area is constant for all precipitates and that the entire lost TA is transformed into aragonite particles, the
145 experimentally determined TA-loss was used to calculate the surface area after each timestep, therefore allowing
146 to correct the precipitation rates.

147

148 **2.4 Particle analysis**

149 The precipitated particles of three filters (0.2 μ m PC), collected during incubation experiments within previous
150 campaigns published in Hartmann et al. (2023) (neq Δ TA₂₄₀₀, Gran Canaria) and Suitner et al. (2024) (neq Δ TA₂₆₀₀
151 and Δ TA₂₈₀₀, Raunefjorden, also see section 2.1). Similar to the incubations from the Raunefjorden, the filters
152 from the Gran Canaria campaign originate from TA-gradient experiment, utilizing the local oligotrophic seawater
153 ($TA_{\text{initial}} \sim 2411 \mu\text{mol kg}^{-1}$, $S \sim 36.6$, $pH \sim 8.15$, $T \sim 23 \text{ }^\circ\text{C}$) to test the stability of alkalization approaches (see SI for
154 further details). The filtered precipitates were analyzed by scanning electron microscopy (SEM; Tabletop
155 Microscope Hitachi TM4000plus - University of Hamburg) to determine shape, size and quantity of the
156 precipitated material. Length, width and shape of each particle were specified by manual examination.
157 If sufficient precipitated materials could be provided, the remaining SEM filter material was used to determine
158 their sinking velocities, utilizing a FlowCam (Fluid Imaging Technologies Inc., Scarborough, United States). A
159 detailed description of the setup is provided in Suessle et al. (2023) and references therein.

160 **3 Results**

161 **3.1 Numerical logistic curve-fittings**

162 Three OAE gradient approaches by Suitner et al. (2024) were examined to test the stability of TA and to generate
 163 refined numerical logistic curve fittings of the temporal development of TA and Ω_{ar} (Figs. 3, S1 and S2). The
 164 coefficients **(b)** and **(c)** (see Fig. 2) were determined by numerical interpolation to optimize the fit to Eq. (1) and
 165 its derivative in equal proportions. Therefore, the shown functions were optimized to describe the temporal
 166 evolution, while also including the rate loss changes, which allowed an improved description of the runaway
 167 process in comparison to the approaches in previous studies. Outlying data points displaying an anomalous
 168 increase or stagnation in values in the filtered approaches were removed from curve-fitting calculations (for
 169 details see SI). For each treatment, continuous differentiable functions to describe and analyze the runaway
 170 carbonate precipitation process during OAE approaches were generated. To illustrate the described processes
 171 and trends, the unfiltered neq approach was selected as an example (Fig. 3). The plots for the filtered approaches
 172 are provided in the SI (Figs. S1, S2 and S3).

173

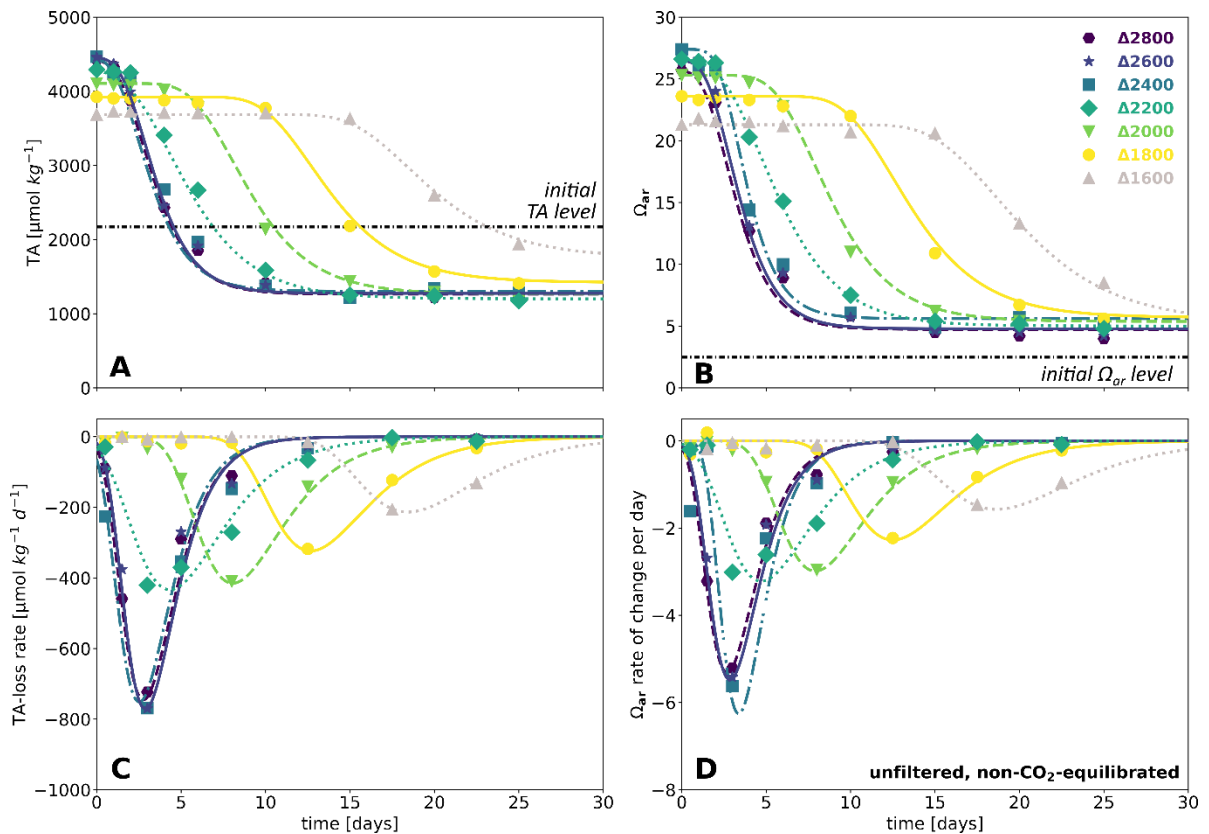


Figure 3: Results of the numerical curve fits – for the unfiltered neq approach, TA evolution over time (A), Ω_{ar} evolution over time (B), TA-loss rate over time (C), Ω_{ar} rate of change over time (D). Line plots: curve-fitted continuous functions, markers: measured data points, for related diagrams for filtered approaches see Figs. S1, S2 and S3.

174

175 For the unfiltered neq experiment (Fig. 3), treatment levels ΔTA_{1600} and higher entered into an APP after
 176 exceeding critical TA levels to initiate the runaway carbonate precipitation process. Treatments levels ΔTA_{2400} -

177 ω_{2600} exhibited a buffering as a consequence of magnesium hydroxide precipitation (see Badjatya et al., 2022;
178 Ringham et al., 2024; Suitner et al., 2024; Varliero et al., 2024), which prevented an increase above $\sim 4470 \mu\text{mol}$
179 kg^{-1} in TA and ~ 27.4 in Ω_{ar} . The buffering effects were not recognized within the fitting procedure and the first
180 data point (after ~ 3 min runtime) of each treatment level was set as the baseline.

181

182 3.2 Induction time and timespan of the APP

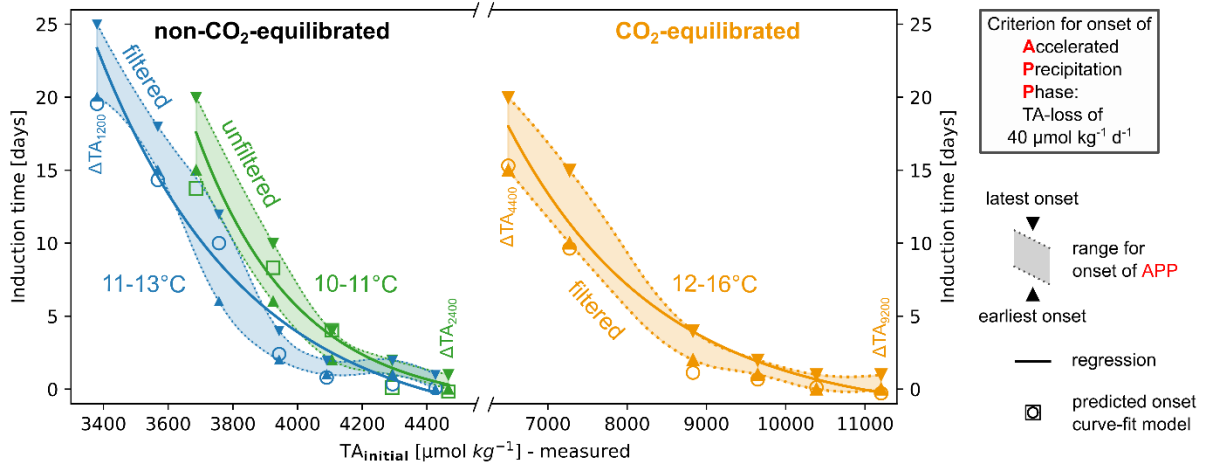
183 By employing the logistic curve fits, the temporal evolution of each approach could be parameterized. To identify
184 the temporal stability ranges and reflect the transition from stable to precipitation-dominated system modes, a
185 criterion of $40 \mu\text{mol kg}^{-1} \text{d}^{-1}$ rate of change in TA was set. This rate provides a sufficiently high threshold to exclude
186 a false detection due to natural variability or measurement errors, while still being low enough not to overlook
187 a significant fraction of TA-loss (see Fig. S11 for varying criteria).

188 Based on this criterion, Fig. 4 illustrates the induction times for the APPs. The shaded ranges indicate
189 extrapolated timeframes between subsequent measurements during which the initiation of the APP for each
190 treatment was detected. The displayed regressions were calculated using the averaged times from two
191 consecutive measurement days. For comparison, hollow markers represent predictions from the presented
192 curve-fitted functions. The regressions of the induction times uniformly follow an inverse exponential trend of
193 the type:

$$194 \quad t(TA) = f e^{-g TA} - h \quad (5)$$

195 The employed data series covered a range of 25 days with progressively increasing induction times from 0 to 20
196 days for treatments reaching ~ 4470 (ΔTA_{2400}) to $\sim 3380 \mu\text{mol kg}^{-1}$ (ΔTA_{1200}) in the filtered neq experiment and
197 ~ 11200 (ΔTA_{9200}) to $\sim 6500 \mu\text{mol kg}^{-1}$ (ΔTA_{4400}) in the filtered eq experiment. Treatment levels above ΔTA_{2400} in
198 the neq approaches exhibited an immediate onset of TA-loss due to the precipitation of secondary hydroxides
199 and/or carbonate minerals, therefore, following the presented criterion, practically leading to their immediate
200 entry into the APP process.

201 The same relationships and trends can also be applied using Ω_{ar} as a variable. While the neq approaches exhibited
202 lower Ω_{ar} values (17.8-27.4) compared to the eq treatments (19.5-43.6), the onset of the APP in the neq
203 experiments occurred significantly earlier. This indicates that Ω_{ar} is not the only decisive factor guiding the
204 (pseudo-) homogeneous nucleation process, determining the induction time.



205 Figure 4: Induction time for the onset of APP in relation to the initial TA addition level, based on the first detection of a TA-loss
 206 rate of $40 \mu\text{mol kg}^{-1} \text{d}^{-1}$. Each pair of triangle markers represents two consecutive measurement days during which the set loss
 207 rate criterion was met; hollow markers: predicted induction times for each treatment level, based on the introduced curve-fit
 208 model. Exponential regression of average experimentally detected induction time, see Eq. (5) in Tab. 2 for related functions.

209

210 Table 2: Regressions of induction times, see Fig. 4. Note that the use of the given equation should not be generalized, as it is
 211 only valid under the presented environmental conditions. Also be aware that the resulting predictions of induction times far
 212 out of the specified TA addition ranges might not be accurate.

$t(TA_{initial}) = f e^{-g TA_{initial}} - h$ (5)			Regression			
Treatment		Temp. [°C]	$f * 10^3$	$g * 10^{-4}$	h	R ²
non- equilibrated	unfiltered	10-11	2721.769	32.233	1.215	0.996
	filtered	11-13	39.633	21.646	2.972	0.977
equilibrated	filtered	12-16	0.603	5.243	1.934	0.988

213

214 3.3 Timespan of APP

215 To describe the temporal evolution of TA and Ω_{ar} during the observed runaway processes for the present setups,
 216 coefficients **(a)** and **(d)** in Eq. (1) can be set, while **(b)** could be evaluated by empirical or modeled data.
 217 Consequently, only the duration of the APP represented by **(c)** needs to be estimated to enable the entire model
 218 description of the precipitation procedure. The discrete nature of sampling days with decreasing frequency of
 219 samplings towards the end of an experiment (up to 5 days) did not allow reliable empirical determinations of **(c)**.
 220 The displayed APP timespans in Fig. 5 were therefore determined by the predictions of the presented curve-fits
 221 (Fig. 3), based on the $40 \mu\text{mol kg}^{-1} \text{d}^{-1}$ TA-loss criterion to define the start and endpoint of the APPs. Fig. 5
 222 illustrates the related predicted timespans against the initially reached TA levels, categorized by the individual
 223 experimental setups. The neq APPs form distinct clusters for each approach, which again can be subdivided into
 224 treatments with and without the occurrence of immediate precipitation. Regardless of the initial TA
 225 enhancement level, treatments that exhibited an immediate decline due to $\text{Mg}(\text{OH})_2$ formation showcased
 226 almost identical APP spans (unfiltered ~ 8.8 and filtered $\sim 5.9-7.4$ days) within each approach. Although the neq
 227 treatments without $\text{Mg}(\text{OH})_2$ had the same starting conditions, the unfiltered experiments exhibited

228 approximately 4 days longer APPs. In the eq approach, the APPs showed a continuous decrease as the initial TA
 229 addition levels increased, ranging from 5 to 11 days.

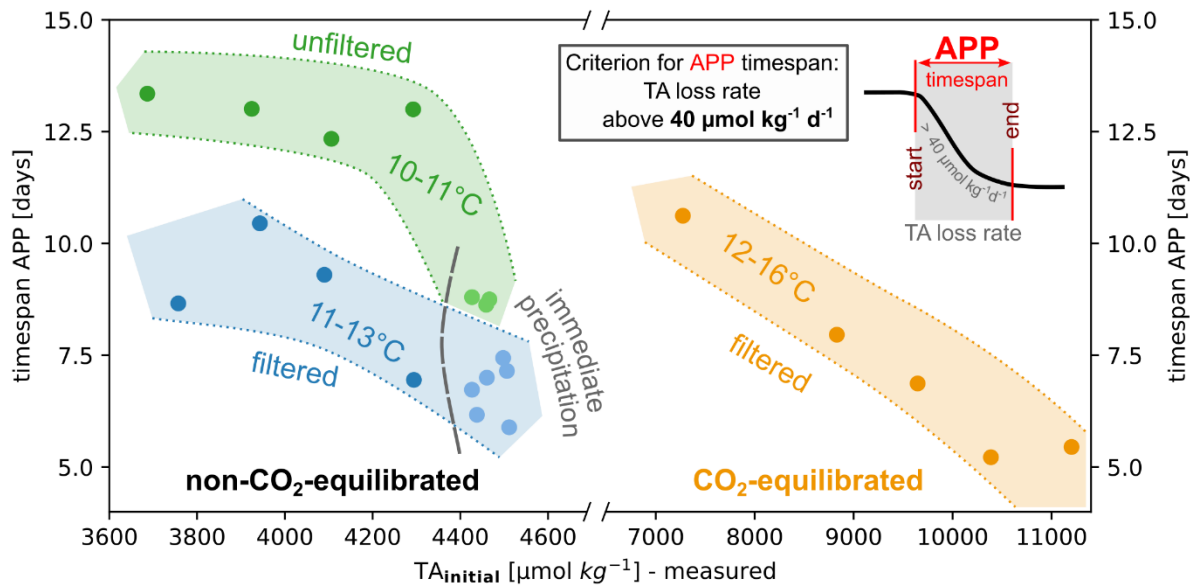
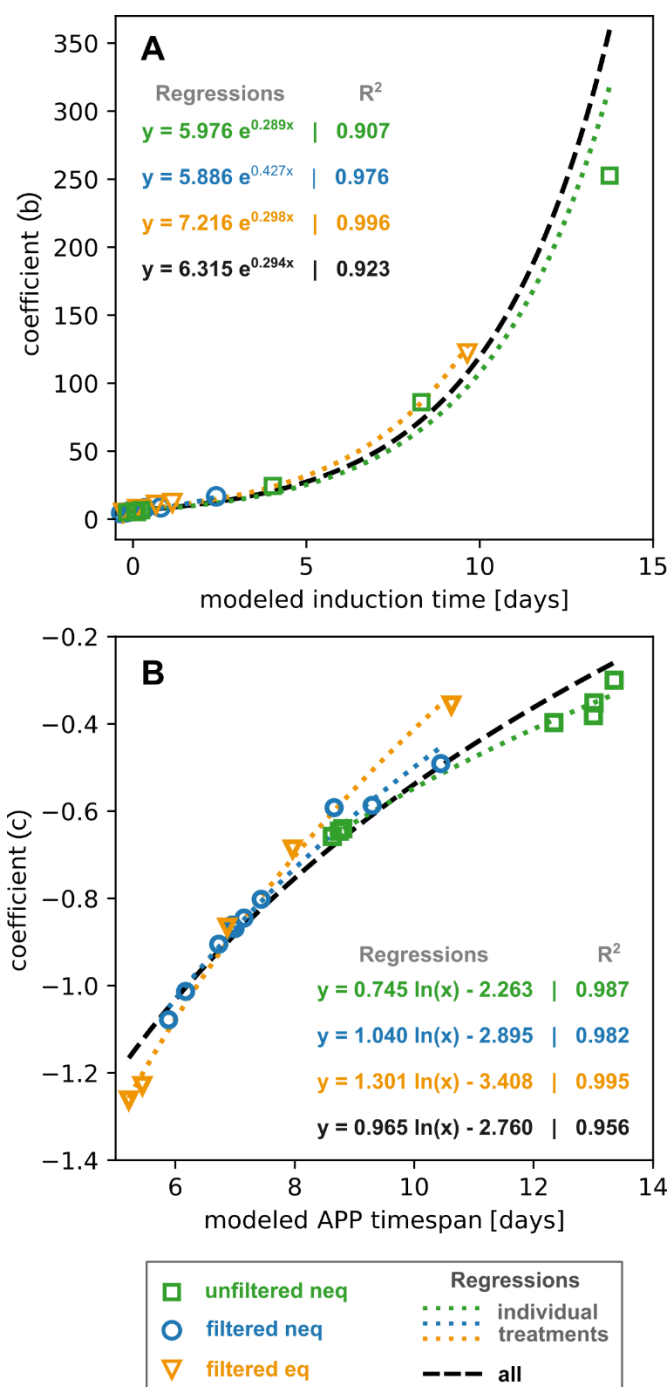


Figure 5: Overview timespans of APP in relation to the initial TA addition level; determined by the outcomes of the presented numerical logistic curve-fitting. Presented timespans are based on the introduced TA-loss criterion (see section 3.2), which was defined as period with rates above $40 \mu\text{mol kg}^{-1} \text{d}^{-1}$; only treatments which reached the final stable stage were considered, neq treatments labeled with immediate precipitation showcased a loss of TA within the first 3 min of the experiment – most likely as a consequence of $\text{Mg}(\text{OH})_2$ formation.

230 3.4 Prediction of onset and timespan of APP

231 The established continuous logistic functions allow estimations of effects occurring between measurement
 232 points, thereby improving the overall accuracy beyond what discrete experimental datasets could provide. Based
 233 on the $40 \mu\text{mol kg}^{-1} \text{d}^{-1}$ TA-loss criterion (see section 3.2 and sketch Fig. 5), these functions could therefore assess
 234 the initiation of the APP for specific initial TA and Ω_{ar} levels, as well as a given starting particle surface area (see
 235 regressions in Fig. 4). In this regard, Fig. 6 illustrates the correlations of the curve-fitted coefficients **(b)** and **(c)**
 236 and their related entities of the modeled induction times and APP timespans (see Fig. 2). Under the present
 237 physicochemical conditions, the provided regressions could be utilized as conversion equations to estimate the
 238 TA development of a treated water mass based on an existing database or to convert observational data into
 239 mathematically expressible equations for predicting the future evolution. Note that the high correlations of
 240 coefficients **(b)** and **(c)** with induction times and APP timespans are relate to the circumstance that both
 241 coefficients are determined through the described numerical curve-fitting procedure, which is based on the
 242 properties of the logistic function and thus indirectly incorporates information about induction times and APP
 243 timespans.

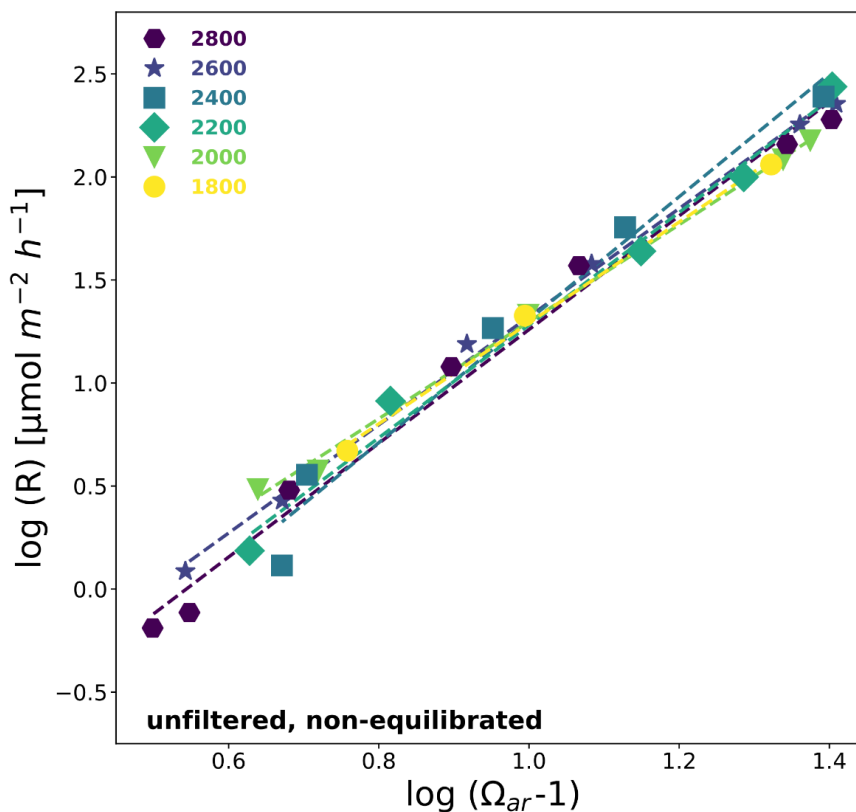
Figure 6: Regressions describing the relationships between the coefficient (b) and the modeled induction time [A], as well as the coefficient (c) and the modeled APP timespan [B] for each approach. The shown regressions allow for the conversion of specifiable time-dependent characteristics of a runaway process to the coefficients of the presented inverse logistic function (Eq. (1)). Specified relationships should not be generalized and are only valid within the given conditions of each approach.



244 3.5 Empirical rate equations

245 Additional insights into the reaction speed and the associated timespan of the APP can be obtained through
 246 analysis of empirical rate law equations. As an example, Fig. 7 illustrates the relationship between the logarithm
 247 of TA-loss rates normalized to the surface area and the aragonite saturation states for the unfiltered neq
 248 approach (see Figs. S4 and S5 for details on the filtered approaches), focusing on treatments that entered the
 249 APP. Throughout all experiments the logarithm of the surface area normalized TA-loss rates R correlates with the
 250 $\log(\Omega_{ar}-1)$, in accordance with similar observations reported in literature (e.g. Morse et al., 2007; Mucci & Morse,
 251 1983; Zhong & Mucci, 1989). The parameters n and k in Eq (2): $R = k(\Omega_{ar}-1)^n$ were determined for each treatment
 252 level in this work, as outlined in Eq (2) to (4) (section 2.3). Here, R represents the surface area normalized TA-loss
 253 rate, and k denotes the rate constant.

254 The values for n and $\log(k)$ derived from the linear regressions in the unfiltered neq treatments are provided in
 255 Tab. 3 (see Tabs. S4 and S5 for filtered experiments). These values demonstrate reasonable consistency in n and
 256 $\log(k)$ within each of the three separate experiments. Treatment levels influenced by the immediate formation
 257 of $\text{Mg}(\text{OH})_2$ as pH approached approximately 10.3 show minor deviations, the remaining treatment levels exhibit
 258 reaction orders (n) within a relatively narrow range of 2.45 to 2.73. In comparison, $\log(k)$ values ranged between
 259 0.30-1.68, showcasing a higher variability.



260 *Figure 7: Carbonate precipitation kinetics for unfiltered neq treatments that entered the APP; see Tab. 3 for related regressions*
 261 *and rate equations.*

262
 263 *Table 3: Overview of coefficients and regressions of empirical rate equations for unfiltered neq treatments, also see Fig. 7 and*
 264 *Tab. S6 for cross-comparison of all treatments.*

Treatment	$\log(R) = n(\Omega_{ar} - 1) + \log(k)$			
ΔT_A	n	$\log(k)$	R^2	$\hat{\sigma}$
2800	2.76	-1.50	0.989	0.117
2600	2.62	-1.30	0.997	0.055
2400	2.98	-1.68	0.975	0.167
2200	2.73	-1.45	0.989	0.106
2000	2.35	-1.06	0.997	0.046
1800	2.45	-1.16	0.996	0.060
all	2.68	-1.39	0.985	0.106

265

266 3.6 Evolution of particles and sinking speed

267 To assess the impact of secondary precipitated particles during OAE approaches, precipitated materials from the
268 studies by Hartmann et al. (2023) and Suitner et al. (2024) were analyzed for shape, size, and sinking velocity. As
269 qualitatively depicted in these studies, the aragonite precipitates manifest and evolve in a variety of forms and
270 sizes, ranging from stem-like structures, followed by double-broccoli shapes and ultimately forming closed
271 spheres (see Fig. 8).

272 For this study the length and width distribution of 950 precipitated particles were determined by manual
273 inspection of four overview SEM images (see Fig. S7) from Gran Canaria samples (see Hartmann et al., 2023 for
274 details; analyzed treatment level: ΔTA_{2400} , filtered, neq, Temp. $\sim 23^\circ\text{C}$, Sal. ~ 36.5 , runtime 4 days) and the
275 Raunefjorden, Bergen (this study and Suitner et al., 2024, see Figs. 3 and 7 therein; analyzed treatment levels:
276 ΔTA_{2800} and ΔTA_{2600} , Temp. $\sim 11^\circ\text{C}$, Sal. 32.6, runtime 25 days – highest unfiltered neq treatments). Results of this
277 evaluation are provided in Fig. S8. Length and width distributions of the formed particles follow distinct ratios,
278 allowing the definition of three categories: **1.** Stems (<0.5), **2.** Broccoli ($0.5 < x < 0.9$) and **3.** Spheres (>0.9). Note
279 that this method also categorizes regularly shaped, multi-branched particles as spheres (see Fig. 8). Precipitates
280 from the Gran Canaria campaign primarily comprised well-developed broccoli and spherical-shaped particles,
281 whereas the samples from the Raunefjorden were characterized by less evolved stems and broccoli as the
282 dominant components. Although the runtime for the Gran Canaria sample was considerably shorter (4 days) in
283 comparison to the Raunefjorden (25 days), the $\sim 12^\circ\text{C}$ difference in temperature led to significantly higher
284 precipitation rates and more developed shapes. The analyzed Raunefjorden samples originate from the same
285 experiment and differ only in the initially added TA-level of $200 \mu\text{mol kg}^{-1}$. Even this minor difference in TA
286 addition resulted in the presence of more evolved shapes in the higher treatment.

287 The gravitational sinking velocities of precipitated particles were measured using a FlowCam setup (see Bach et
288 al., 2012 for technical details). Based on the concept of equivalent spherical diameters (ESD) the density of each
289 particle was calculated, revealing a range from 1.54 to 3.18 g cm^{-3} for ESD sizes between 12 and $50 \mu\text{m}$. The
290 average density was determined to be 2.358 g cm^{-3} . The discrepancy with the density of aragonite ($\sim 2.95 \text{ g cm}^{-3}$)
291 may result from an overestimation of particle sizes in the calculation method, which relies on an inversion of
292 Stokes' Law for the terminal sinking velocity of perfect spheres. However, most particles are non-spherical and
293 contain numerous internal cavities within their structure (see Fig. S7), and their densities are therefore expected
294 to be lower than those of pure aragonite. The determined particle density was then used to calculate the
295 theoretical sinking velocities of the manually counted precipitated particles. To account for potential variability
296 in particle density, Fig. 8 presents a range of sinking velocities of the counted precipitates.

297 Measured sinking velocities for precipitated particles within the aforementioned density range varied from $\sim 5 \text{ m}$
298 d^{-1} ($14 \mu\text{m}$ particle) to $\sim 47 \text{ m d}^{-1}$ ($41 \mu\text{m}$ particle). Recorded particles in the ESD range of 50 - $180 \mu\text{m}$ were not
299 included in the calculations, as they were not observed within the same filter material that was analyzed by visual
300 inspection. Discrepancies between measured and calculated values may reflect aggregation effects or technical
301 limitations of the utilized FlowCam to track particles smaller than $3 \mu\text{m}$ (Bach et al., 2012).

302 Derived from the calculated sinking velocities, the residence times within the upper 200 m of the water column
303 were determined. Accordingly, under idealized conditions, early precipitated stages, such as stems ($<10\mu\text{m}$),

304 could remain for a few months within the upper ocean layer, providing potential additional surfaces for an
305 ongoing heterogeneous precipitation if a continuous local alkalization is applied. In contrast, precipitates >30
306 μm would descend within days to deeper ocean layers, not affecting the precipitation behavior of continuous
307 surface alkalization attempts. Notice that sinking velocities are temperature and salinity dependent, and
308 therefore would vary under different environmental conditions (see Fig. S9).

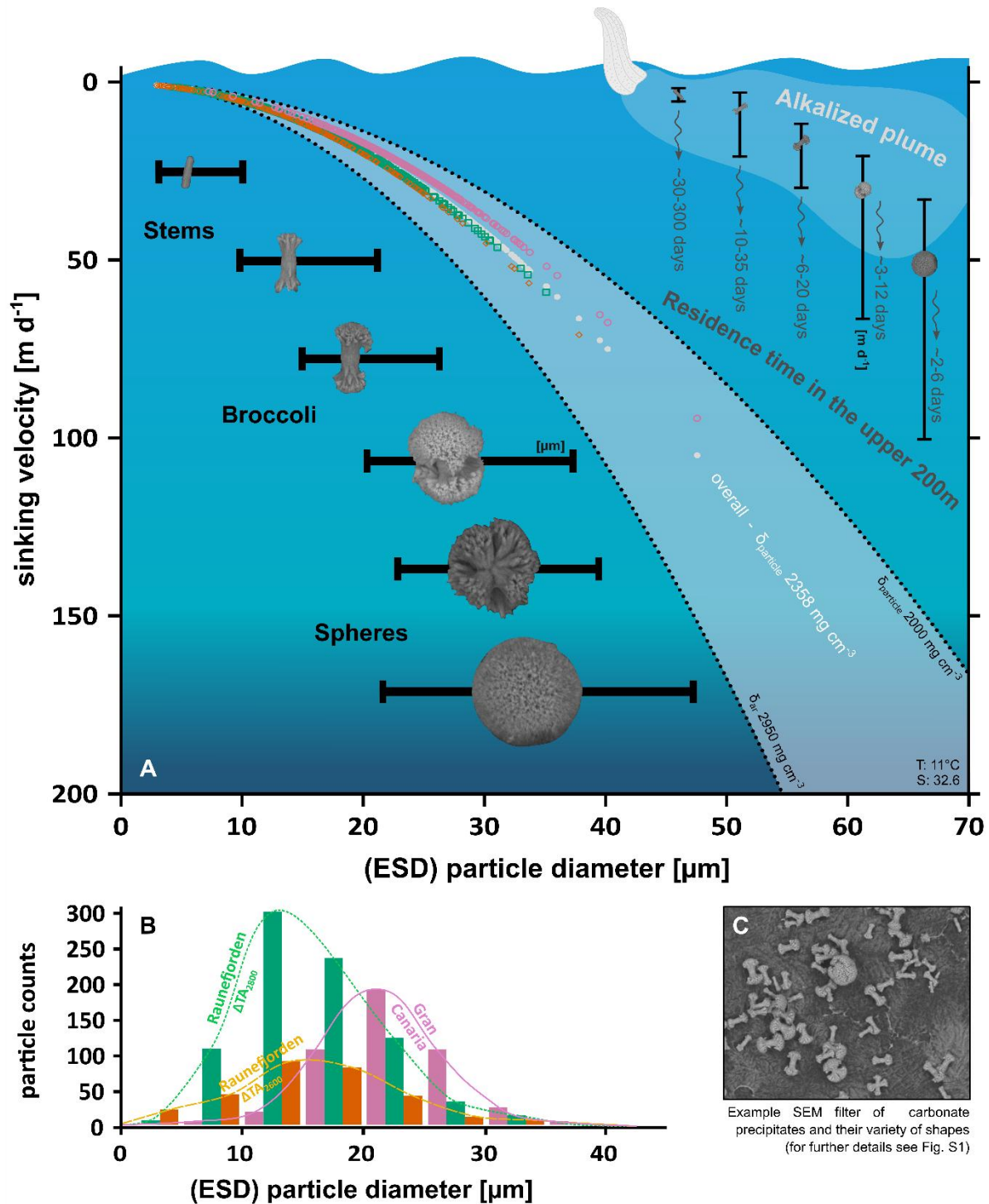


Figure 8: (A) Calculated sinking velocities of particles (hollow markers) as a function of ESD for each treatment (green squares: neq unfiltered ΔTA_{2800} – Raunefjorden, Bergen; orange diamonds: neq unfiltered ΔTA_{2600} Raunefjorden, Bergen; pink circles: neq filtered ΔTA_{2400} Gran Canaria). ESD distribution of stem, broccoli and sphere shaped precipitates (horizontal) and their calculated mean residence time in the mixed layer (assumed to be 200 m), while neglecting particle growth processes (B) related particles counts in size fractions of 5 μm , also see Fig. S8 for length:width distribution (C) example section of a SEM filter (ΔTA_{2600} Raunefjorden), see Fig. S7 for complete set of all filters.

310 **4 Discussion**

311 **4.1 General findings**

312 By analyzing the experimental datasets provided by Suitner et al. (2024), this study demonstrates that the
313 process of TA-loss during runaway carbonate precipitation follows quantifiable relationships. For the present
314 study, the compiled concepts allowed the description of the principles guiding the entire runaway process. The
315 obtained capability to predict TA-stability ranges, in terms of time and magnitude, might help prevent secondary
316 mineral formation, thereby optimizing the assessments for OAE application scenarios. Furthermore, the
317 simplicity of the logistic curve fit model, along with the demonstration that the carbonate precipitation follows
318 simple rate law equations (see Morse et al., 2007; Mucci & Morse, 1983; Zhong & Mucci, 1989), might facilitate
319 the straightforward integration of these fundamental mechanisms into ocean models like the studies by He &
320 Tyka (2023), Ou et al. (2025), Schwinger et al. (2024), Wang et al. (2022) or Zhou et al. (2024).

321

322 **4.2 Nucleation and onset of accelerated precipitation phase**

323 Previous studies examining the evolution of the runaway precipitation process in the context of OAE (Hartmann
324 et al., 2023; Moras et al., 2022, 2024; Suitner et al., 2024) observed and described considerable periods with
325 stable TA levels before the onset of the APP (see Fig. 1), depending on the TA and DIC levels.

326 In theory, even at natural background supersaturation levels in the ocean, (pseudo-)homogeneous precipitation
327 is expected to occur at very slow rates, on timescales of thousands of years (Pytkowicz, 1965, 1973). Regardless,
328 the nucleation and precipitation processes in ocean waters are suppressed by inhibitory species like Mg^{2+}
329 (Berner, 1975; Pan et al., 2021; Pokrovsky, 1998), phosphate- (Burton & Walter, 1990) or dissolved organic
330 matter (Chave & Suess, 1970; Kellock et al., 2022; Moras et al., 2024). Naturally occurring precipitation events in
331 the ocean are associated with unique occurrences such as flash floods (Wurgaft et al., 2016, 2021) or observed
332 during whiting events (Broecker & Takahashi, 1966; Bustos-Serrano et al., 2009; Morse et al., 2003), providing
333 high degrees of (re)suspended sediments that catalyze a heterogeneous carbonate precipitation procedure.

334 To consider the persistent (pseudo-)homogeneous precipitation within typical natural seawater supersaturation
335 ranges, the terminology concerning specific stability ranges of TA or timeframes for the onset of secondary
336 carbonate formation should be refined. However, within typical observation times in the Earth system, the
337 precipitation of secondary calcium carbonate in particle-free seawater solutions is expected to be suppressed to
338 Ω_{ar} values of approximately 11.3 or below (derived from Eq. (4) in Marion et al. (2009), based on data by Morse
339 & He (1993) and Morse et al. (2007)).

340 Nevertheless, even a 0.2 μ m-filtered natural seawater contains around $\sim 10^9$ particles per ml in the size range of
341 5-120 nm, already offering a total surface area of around 8 m² per m³ (cf. Wells & Goldberg, 1992), potentially
342 acting as a catalyst to initiate carbonate precipitation in alkalinity treated seawater. In the presence of surfaces
343 for pseudo-homogeneous/ heterogeneous precipitation such as suspended sediments, colloids, organic matter
344 or the introduced solid alkalization substrates, Moras et al. (2022) reported an Ω_{ar} threshold of $\sim 5-7$ for the
345 observable onset of carbonate formation for the given runtime of the experiment. Potentially, the colloidal

346 structure of $\text{Mg}(\text{OH})_2$ precipitates (see Badjatya et al., 2022), typically formed above pH values of ~ 10.5 as a
347 consequence of TA addition (cf. Eisaman et al., 2023; Haas, 1916; Kapp, 1928; Suitner et al., 2024; Varliero et al.,
348 2024) could serve the same purpose and lower the threshold for carbonate precipitation. However, the
349 redissolution of the formed $\text{Mg}(\text{OH})_2$ through the mixing and dilution processes, as described by Ringham et al.
350 (2024), may inhibit this effect and would also allow much higher short-term pH and TA concentrations around
351 an alkalinity injection site when using liquid stock solutions.

352 To characterize the transition from a state with negligible shifts in carbonate chemistry towards a phase primarily
353 driven by carbonate formation, a practicable criterion of a $40 \mu\text{mol kg}^{-1} \text{d}^{-1}$ TA-loss was set to determine the start
354 of the intensified precipitation stage (see Figs. 4 and 5). This criterion was also used to describe the induction
355 time, which is the period before a measurable onset of secondary carbonate formation can be detected (Fig. 4).
356 Since the induction time includes a fundamental uncertainty, it does not reflect an intrinsic property of the
357 treated solution itself and relies on the detection capability of the experimental setup (Söhnel & Mullin, 1988)
358 and might be chosen differently in future work (see Fig. S11 for varying criteria). While the selected criterion
359 already depicts relatively high loss rates, it enables detectable changes, distinguishable from measurement
360 uncertainties or natural variabilities. The overall emerging patterns related to the onset and duration of the APP
361 nevertheless remained relatively consistent across different tested threshold values.

362

363 **4.3 Predictability of the runaway process**

364 The consistent patterns during the TA-loss within all three experimental setups allowed the introduction of
365 continuous and differentiable functions for each treatment level, enabling further analysis to examine relevant
366 factors guiding the runaway process. Fuhr et al. (2022) utilized a comparable inverted logistic function to model
367 the process of secondary carbonate formation during olivine dissolution experiments in seawater. However, the
368 model was not consistently applied to describe a runaway carbonate precipitation process nor used as a general
369 predictive model to determine the stability ranges of the added TA in OAE approaches.

370 The characteristics of the logistic function applied in this study, facilitate the conversion of both empirically
371 determined and hypothetical parameters, such as induction time, duration of the APP (Fig. 5), or the initial and
372 final TA levels before and after the runaway process. The applicability of kinetic rate equations, combined with
373 the ability to quantify the precipitation process, enables a description and prediction of the temporal evolution
374 of the carbonate formation. This may facilitate the integration of the TA depletion procedure into various
375 predictive modeling approaches. Although these statements currently apply only under the tested
376 environmental conditions, they nonetheless suggest the general capability to assess a framework for guiding
377 time and TA level ranges in OAE approaches. Since the logistic model is based on experimental data from bottle
378 experiments, processes such as the removal of surface area due to the sinking of precipitated carbonate particles
379 were not accounted for - see section 4.6 for an approach to address this topic.

380 Under specified temperature and salinity conditions, as well as predefined TA/DIC levels after OAE treatment
381 and an estimated final Ω_{ar} after the precipitation process stopped (typically ~ 1.5 - 5.0 , see Fuhr et al., 2022;
382 Hartmann et al., 2023; Moras et al., 2022; Pan et al., 2021; Suitner et al., 2024), the resulting total TA-loss can be
383 computed. This calculation follows the condition that the TA-loss reflects the ideal 2:1 TA:DIC ratio during

384 carbonate mineral precipitation in seawater (Zeebe & Wolf-Gladrow, 2001). Given these assumptions, upper and
385 lower limits of the logistic function (coefficients **(a)** and **(d)**, Eq. (1)) can be determined. To characterize measures
386 such as induction time (coefficient **(b)**) and the duration of the APP (coefficient **(c)**), it is necessary to acquire
387 empirical data that account for the specific conditions of the deployment area. These data could either be
388 provided by actual experiments or model predictions, based on a comprehensive database which accounts for
389 broad ranges of TA, DIC, temperature, salinity, and practical available surface area, as well as inhibitory factors
390 or potential effects of biota. To validate the predicted precipitation behavior, additional gradient experiments
391 need to be conducted to better understand the geochemical reaction pathways.

392

393 **4.4 Empirical rate equations using Ω_{ar} and particle surface area during APP**

394 After passing the induction time to start the detectable carbonate formation process by (pseudo-/)homogeneous
395 precipitation and overcoming the delaying inhibition effects (Marion et al., 2009; Morse & He, 1993; Schulz et
396 al., 2023), the triggered heterogeneous precipitation can be described by basic empirical rate equations (Fig. 7,
397 S4 and S5). These equations demonstrate the fundamental role of Ω_{ar} as a guiding factor for the precipitation
398 process. The kinetics of carbonate formation remained relatively consistent across all treatment levels within
399 each experimental approach (see Tabs. 3, S4 and S5). The observed consistent correlations between saturation
400 states and surface area normalized precipitation rates indicate that the runaway carbonate formation processes
401 during the present incubations followed the known kinetics of heterogeneous carbonate formation in seawater
402 (cf. Morse et al., 2007; Zhong & Mucci, 1989).

403 Fig. 9 illustrates the role of Ω_{ar} saturation states and generated particle surface area in guiding the TA-loss rates
404 during the precipitation process. The black line represents the curve fit of TA-loss rates of the unfiltered neq
405 ΔTA_{2000} approach; the experimentally determined rates are indicated by black triangles (also see Fig. 3c).
406 Assuming that the entire lost TA was transformed into aragonite precipitates with a surface area of $2.283 \text{ m}^2 \text{ g}^{-1}$
407 (see section 2.3), the total generated particle surface area (PSA) could be determined (red, dash-dotted line).
408 The overall expected TA-loss rate per m^2 (brown, dashed line) was obtained by utilizing the empirical logistic
409 curve fit for the temporal evolution of Ω_{ar} (Fig. 3b), normalizing it to 1 m^2 surface area, and inserting it into the
410 rate equation (Eq. (4)). Given that the system initially exhibits a negligible degree of PSA, the relatively high
411 precipitation potential by the Ω_{ar} saturation state does not result in a measurable TA-loss rate. Following the
412 presented concept, the consistently high Ω_{ar} values led to a continuous (pseudo-/)homogeneous precipitation
413 during the induction time, thus causing a rise in PSA until the system shifts to heterogeneous precipitation, and
414 ultimately resulting in a detectable exponential runaway process. The interplay of precipitation potential by Ω_{ar}
415 and the practical available surface area could therefore be determined as the primary factors guiding the actual
416 observed TA-loss rates.

417 Within the uncertainties of the applied calculation steps and methods, the practical TA-loss rate could simply be
418 described as the product of these two factors. To visualize this relationship, the dotted light blue line in Fig. 9
419 represents an empirical rate law equation that combines the shown PSA (red, dash-dotted line) and the surface
420 normalized expected precipitation rate (brown, dashed line) with the determined rate constant (k) and reaction
421 order (n) for the ΔTA_{2000} treatment (see Tab. 3). The shape of the resulting function traces the measured TA-loss

422 rates (black triangles) within reasonable accuracy (see Fig. S10 for other treatments). Be aware that any kind of
 423 inhibition effect is incorporated in the underlying experimentally determined temporal TA evolution which
 424 represents the basis for all shown parameters.

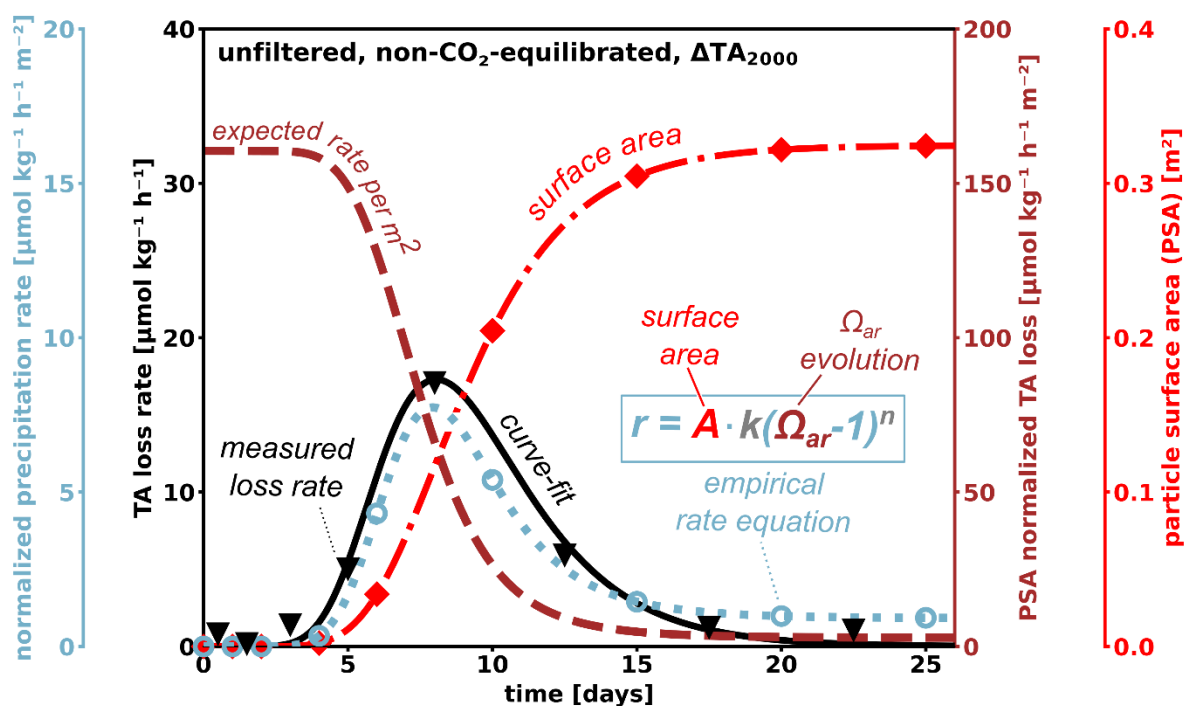


Figure 9: Conceptual figure, illustrating the interplay of Ω_{ar} and particle surface area guiding the TA-loss rate evolution (dashed, brown). After TA injection high Ω_{ar} values provide a high potential for the formation of carbonates by heterogeneous precipitation. In the absence of existing particle surface area (red dash-dotted), (pseudo-)homogenous precipitation would dominate the period until the start of the APP and the resulting runaway precipitation process. Observed TA-loss rates (black triangles) are therefore a combination of the available practical surface area and the precipitation potential by Ω_{ar} oversaturation. The related empirical rate equation (dotted, light blue) connects these two factors with the determined rate constant (k) and reaction order (n), tracing the shape and symmetry of the measured TA-loss rate. Hollow light-blue markers provide the output of the related empirical rate equations for each sampling day. While the potential to precipitate carbonates decreases with progressive precipitation, additional surface area is generated. Understanding how long particles remain in a critical zone to maintain a full-grown runaway process is therefore relevant for future considerations. The shown TA and loss rate data are taken from the empirical data sets for the neq unfiltered ΔTA₂₀₀₀ approach, see Fig. S10 for other treatments levels.

425

426 **4.5 Could a runaway process be triggered in an open world context?**

427 Mixing with untreated water around an injection point may lead to an efficient dilution below non-critical TA
 428 levels within seconds to minutes. Such a process would effectively prevent TA leakage, as described in this study,
 429 which assumes that the formed particles act as catalysts for future precipitation. This is supported by findings
 430 from a mesocosm experiment and corresponding side experiments, where the presence of additional suspended
 431 aragonite particles accelerated the TA-loss (Paul et al., 2024). In contrast, fresh seawater enhanced to the same
 432 TA-levels did not show any TA-loss within 10 days in their experiments. These observations indicate that free-
 433 floating particles in the water column can accelerate heterogeneous precipitation in a runaway style.

434 Precipitation events can be triggered naturally without additional treatment, especially for locations with already
435 relatively high Ω_{ar} background levels, for example, due to high evaporation rates (Bialik et al., 2022) or high
436 degrees of (re)suspended sediments present on carbonate platforms (Broecker & Takahashi, 1966; Bustos-
437 Serrano et al., 2009; Morse et al., 2003), or close to river mouths (Wurgaft et al., 2016, 2021) providing additional
438 PSA to catalyze precipitation events. Under inappropriate TA deployment circumstances, secondary mineral
439 formation might be triggered locally around injection sites, within short timescales. Moras et al. (2022) suggested
440 that visible APP starts around Ω_{ar} of 5, which translates for the mostly particle-free water of the Raunefjorden
441 into $\Delta TA \sim 245 \mu\text{mol kg}^{-1}$ applying a neq OAE approach and $\Delta TA \sim 580 \mu\text{mol kg}^{-1}$ for an eq OAE approach. The
442 induction time before the APP begins can be estimated using Equation (5), based on the specified TA-loss
443 criterion of $40 \mu\text{mol kg}^{-1} \text{d}^{-1}$. For these configurations, the projected induction times would be 1074 days and 143
444 days, respectively. However, the predicted induction times lie far outside the calibration ranges specified in this
445 study and may therefore be inaccurate. Nevertheless, since these projected APP induction times are also within
446 the suggested residence times of treated water in the upper ocean layers, it is necessary to conduct studies
447 lasting at least for the projected timespans, depending on the local environmental conditions.

448 Significantly shorter induction times were identified for subtropical conditions (Temp. $\sim 23^\circ\text{C}$, Sal. ~ 36 psu, TA
449 $\sim 2400 \mu\text{mol kg}^{-1}$). Hartmann et al. (2023) described an onset of the precipitation after just 4 days for a $50 \mu\text{m}$
450 filtered neq incubation with initial values of $1050 \mu\text{mol kg}^{-1}$ for ΔTA and ~ 15 for Ω_{ar} . Within the same setting,
451 Paul et al. (2024) observed aragonite formation for a CO_2 equilibrated setup with $\Delta TA \sim 2300 \mu\text{mol kg}^{-1}$ and Ω_{ar}
452 9.74 ± 0.15 in mesocosms after 21 days.

453 The upper end members of TA perturbations presented in this study (neq: $\Delta TA > 2400 \mu\text{mol kg}^{-1}$; eq: $\Delta TA > 9000$
454 $\mu\text{mol kg}^{-1}$) are not expected to represent realizable target background values for permanent open world
455 scenarios, which would likely be aligned with biological compatibility. High perturbations would just occur within
456 short timeframes in the near field of an injection site or within enclosed environments without sufficient
457 potential for dilution with untreated water. The implemented gradient approach allowed to examine the
458 principles of secondary carbonate formation under controlled conditions. While such small-scale incubations
459 provide only a limited analogue for natural systems, they nonetheless permit the investigation of fundamental
460 processes in a well-controlled setup.

461

462 **4.6 Consequence of sinking particles removing surface area for carbonate formation**

463 Because the TA-loss rate is proportional to the surface area of particles (Eq. (4)), removal of particles due to
464 sinking processes or dilution with untreated water would result in slower precipitation rates. Small, formed
465 particles may remain in the upper layer for several months (Fig. 8), while medium-sized particles may leave the
466 treated water within a couple of days, depending on temperature and salinity conditions (Figs. 8 and S9). Particles
467 larger than $15 \mu\text{m}$ are expected to sink within one day under the environmental conditions of the Raunefjorden.
468 If those particles were removed by sinking while they were still growing, it can be estimated that approximately
469 30-40% of the available surface area would be removed from the upper 10 m of the water column within one
470 day (also see SI). This would decrease the precipitation rate accordingly as surface area and formation rates are
471 linearly proportional. In a natural open ocean environment, the formation and sinking of precipitates are likely

472 to interact with the existing background of organic and inorganic particles. While any type of particles could
473 potentially serve as nucleation sites, aggregation would increase the sinking speed. These processes were not
474 included in the current model calculations but may be relevant under different conditions. In general, the
475 abundance and sinking of particles need to be addressed if the stability or loss of is to be assessed with a high
476 level of confidence.

477 Efficient dilution of the treated water parcels could therefore significantly reduce ongoing precipitation,
478 especially if the onset of the APP is initiated within the first few seconds. For example, this could be the case in
479 the wake of a ship, in OAE applications utilizing existing marine traffic to distribute TA throughout the world's
480 oceans (Caserini et al., 2021). However, particle-based alkalization approaches would nevertheless temporarily
481 introduce additional surface area until its complete dissolution, and may cause the shift into the APP (Hartmann
482 et al., 2023).

483 **5 Conclusion**

484 TA leakage due to oversaturation sets a limit to the efficiency of OAE approaches. So far, the drivers of the
485 process could not be quantified, preventing the implementation of TA-loss terms in applicability assessments for
486 OAE. An induced runaway process follows predictable patterns that can be modeled using available surface area
487 and aragonite oversaturation, identified as the main factors for the given environmental settings.

488 However, it is expected that parameterizations will systematically change along temperature and salinity
489 gradients, as well as with naturally occurring variations in particle abundance and quality. The determination of
490 their impact was not within the scope of this work, instead this study aimed to provide a framework for how such
491 needed parameterization can be achieved. Achieving a predictability of the induced TA-loss on a global scale
492 would allow the identification of suitable locations for OAE or optimizing applications. Therefore, further
493 research across salinity and temperature gradients would also enhance the predictive capabilities of ocean
494 models. Runaway TA-loss processes, as described in this study, would be significantly altered under natural
495 conditions by dilution and particle export processes. If sinking of particles and dilution with untreated water are
496 considered, the limitations of laboratory bottle experiments become evident. Nevertheless, they contribute
497 valuable parameterizations for model development. Field experiments are necessary to evaluate the validity of
498 the presented theoretical model framework with respect to dilution and particle sinking processes.

499

500 **Data availability**

501 All datasets will be made available at the time of publication.

502 **Author contributions**

503 The idea for this work was conceived by NS, with contributions by JH and SV. NS, SV and PS performed the surface
504 area- and sinking velocity/density measurements. NS interpreted the data with help from all co-authors. NS and
505 JH wrote the text with contributions from all co-authors.

506 **Acknowledgements**

507 Peggy Bartsch (UHH), Carl Lim (UHH) and Julieta Schneider (GEOMAR) are thanked for supporting the preparation
508 and execution of the experiments.

509 **Financial support**

510 This research has been supported by the German Federal Ministry of Education and Research through the
511 CDRmare projects RETAKE-1: grant no. 03F0895F and RETAKE-2: grant no. 03F0965F; Horizon 2020 (OceanNETs;
512 grant no. 869357); the Deutsche Forschungsgemeinschaft (grant no. 390683824), under Germany's Excellence
513 Strategy (EXC 2037, "CLICCS"; grant no. 390683824) contribution to the Center for Earth System Research and
514 Sustainability (CEN) of the University of Hamburg, as well as the Ocean Alk-Align project funded by the Carbon
515 to Sea Initiative.

516 **Competing interests**

517 JHA is consulting the Planeteers GmbH. The contact authors have declared that all other authors have no
518 competing interests.

519 **References**

- 520 Bach, L. T., Riebesell, U., Sett, S., Febiri, S., Rzepka, P., & Schulz, K. G. (2012). An approach for particle sinking
521 velocity measurements in the 3–400 µm size range and considerations on the effect of temperature on
522 sinking rates. *Marine Biology*, 159(8), 1853-1864. <https://doi.org/10.1007/s00227-012-1945-2>
- 523 Badjatya, P., Akca, A. H., Fraga Alvarez, D. V., Chang, B., Ma, S., Pang, X., Wang, E., van Hinsberg, Q., Esposito, D.
524 V., & Kawashima, S. (2022). Carbon-negative cement manufacturing from seawater-derived magnesium
525 feedstocks. *Proc Natl Acad Sci U S A*, 119(34), e2114680119.
526 <https://doi.org/https://doi.org/10.1073/pnas.2114680119>
- 527 Berner, R. A. (1975). The role of magnesium in the crystal growth of calcite and aragonite from sea water.
528 *Geochimica et Cosmochimica Acta*, 39(4), 489-504. [https://doi.org/https://doi.org/10.1016/0016-
529 7037\(75\)90102-7](https://doi.org/https://doi.org/10.1016/0016-7037(75)90102-7)
- 530 Bialik, O. M., Sisma-Ventura, G., Vogt-Vincent, N., Silverman, J., & Katz, T. (2022). Role of oceanic abiotic
531 carbonate precipitation in future atmospheric CO₂ regulation. *Sci Rep*, 12(1), 15970.
532 <https://doi.org/https://doi.org/10.1038/s41598-022-20446-7>
- 533 Broecker, W. S., & Takahashi, T. (1966). Calcium carbonate precipitation on the Bahama Banks. *Journal of*
534 *Geophysical Research*, 71(6), 1575-1602. <https://doi.org/https://doi.org/10.1029/JZ071i006p01575>
- 535 Brunauer, S., Emmett, P. H., & Teller, E. (1938). Adsorption of gases in multimolecular layers. *Journal of the*
536 *American chemical society*, 60(2), 309-319.
- 537 Burton, E. A., & Walter, L. M. (1990). The role of pH in phosphate inhibition of calcite and aragonite precipitation
538 rates in seawater. *Geochimica et Cosmochimica Acta*, 54(3), 797-808.
539 [https://doi.org/https://doi.org/10.1016/0016-7037\(90\)90374-T](https://doi.org/https://doi.org/10.1016/0016-7037(90)90374-T)
- 540 Bustos-Serrano, H., Morse, J. W., & Millero, F. J. (2009). The formation of whittings on the Little Bahama Bank.
541 *Marine Chemistry*, 113(1-2), 1-8. <https://doi.org/https://doi.org/10.1016/j.marchem.2008.10.006>
- 542 Caserini, S., Pagano, D., Campo, F., Abbà, A., De Marco, S., Righi, D., Renforth, P., & Grosso, M. (2021). Potential
543 of Maritime Transport for Ocean Liming and Atmospheric CO₂ Removal. *Frontiers in Climate*, 3.
544 <https://doi.org/https://doi.org/10.3389/fclim.2021.575900>
- 545 Chave, K. E., & Suess, E. (1970). Calcium Carbonate Saturation in Seawater: Effects of Dissolved Organic Matter.
546 *Limnology and Oceanography*, 15(4), 633-637.
547 <https://doi.org/https://doi.org/10.4319/lo.1970.15.4.0633>
- 548 Eisaman, M., Geilert, S., Renforth, P., Bastianini, L., Campbell, J., Dale, A., Foteinis, S., Grasse, P., Hawrot, O., &
549 Löscher, C. (2023). Chapter 3: Assessing the technical aspects of OAE approaches. *State of the Planet*
550 *Discussions*, 2023, 1-52. <https://doi.org/https://doi.org/10.5194/sp-2-0ae2023-3-2023>
- 551 Faucher, G., Haunost, M., Paul, A. J., Tietz, A. U. C., & Riebesell, U. (2024). Growth response of *Emiliania huxleyi*
552 to ocean alkalinity enhancement. *EGU sphere*, 2024, 1-17. [https://doi.org/10.5194/egusphere-2024-
553 2201](https://doi.org/10.5194/egusphere-2024-2201)
- 554 Ferderer, A., Chase, Z., Kennedy, F., Schulz, K. G., & Bach, L. T. (2022). Assessing the influence of ocean alkalinity
555 enhancement on a coastal phytoplankton community. *Biogeosciences*, 19(23), 5375-5399.
556 <https://doi.org/10.5194/bg-19-5375-2022>
- 557 Fuhr, M., Geilert, S., Schmidt, M., Liebetrau, V., Vogt, C., Ledwig, B., & Wallmann, K. (2022). Kinetics of Olivine
558 Weathering in Seawater: An Experimental Study. *Frontiers in Climate*, 4.
559 <https://doi.org/https://doi.org/10.3389/fclim.2022.831587>
- 560 Fuss, S., Lamb, W. F., Callaghan, M. W., Hilaire, J., Creutzig, F., Amann, T., Beringer, T., de Oliveira Garcia, W.,
561 Hartmann, J., Khanna, T., Luderer, G., Nemet, G. F., Rogelj, J., Smith, P., Vicente, J. L. V., Wilcox, J., del
562 Mar Zamora Dominguez, M., & Minx, J. C. (2018). Negative emissions—Part 2: Costs, potentials and side
563 effects. *Environmental Research Letters*, 13(6). <https://doi.org/10.1088/1748-9326/aabf9f>
- 564 Gately, J. A., Kim, S. M., Jin, B., Brzezinski, M. A., & Iglesias-Rodriguez, M. D. (2023). Coccolithophores and diatoms
565 resilient to ocean alkalinity enhancement: A glimpse of hope? *Science Advances*, 9(24), eadg6066.
566 <https://doi.org/10.1126/sciadv.adg6066>
- 567 Goldenberg, S. U., Riebesell, U., Brüggemann, D., Börner, G., Sswat, M., Folkvord, A., Couret, M., Spjelkavik, S.,
568 Sánchez, N., Jaspers, C., & Moyano, M. (2024). Early life stages of fish under ocean alkalinity
569 enhancement in coastal plankton communities. *Biogeosciences*, 21(20), 4521-4532.
570 <https://doi.org/10.5194/bg-21-4521-2024>
- 571 Haas, A. R. (1916). The Effect of the Addition of Alkali to Sea Water Upon the Hydrogen Ion Concentration. *Journal*
572 *of Biological Chemistry*, 26(2), 515-517. [https://doi.org/https://doi.org/10.1016/s0021-9258\(18\)87433-
573 6](https://doi.org/https://doi.org/10.1016/s0021-9258(18)87433-6)

574 Hartmann, J., Suitner, N., Lim, C., Schneider, J., Marín-Samper, L., Arístegui, J., Renforth, P., Taucher, J., &
575 Riebesell, U. (2023). Stability of alkalinity in ocean alkalinity enhancement (OAE) approaches –
576 consequences for durability of CO₂ storage. *Biogeosciences*, 20(4), 781-802.
577 <https://doi.org/https://doi.org/10.5194/bg-20-781-2023>

578 Hartmann, J., West, A. J., Renforth, P., Köhler, P., De La Rocha, C. L., Wolf-Gladrow, D. A., Dürr, H. H., & Scheffran,
579 J. (2013). Enhanced chemical weathering as a geoengineering strategy to reduce atmospheric carbon
580 dioxide, supply nutrients, and mitigate ocean acidification. *Reviews of Geophysics*, 51(2), 113-149.
581 <https://doi.org/https://doi.org/10.1002/rog.20004>

582 Harvey, L. D. D. (2008). Mitigating the atmospheric CO₂ increase and ocean acidification by adding limestone
583 powder to upwelling regions. *Journal of Geophysical Research: Oceans*, 113(C4).
584 <https://doi.org/10.1029/2007jc004373>

585 He, J., & Tyka, M. D. (2023). Limits and CO₂ equilibration of near-coast alkalinity enhancement. *Biogeosciences*,
586 20(1), 27-43. <https://doi.org/https://doi.org/10.5194/bg-20-27-2023>

587 Ilyina, T., Six, K. D., Segschneider, J., Maier-Reimer, E., Li, H., & Núñez-Riboni, I. (2013). Global ocean
588 biogeochemistry model HAMOCC: Model architecture and performance as component of the MPI-Earth
589 system model in different CMIP5 experimental realizations. *Journal of Advances in Modeling Earth
590 Systems*, 5(2), 287–315. <https://doi.org/https://doi.org/10.1029/2012ms000178>

591 Inskeep, W. P., & Bloom, P. R. (1985). An evaluation of rate equations for calcite precipitation kinetics at pCO₂
592 less than 0.01 atm and pH greater than 8. *Geochimica et Cosmochimica Acta*, 49(10), 2165-2180.
593 [https://doi.org/https://doi.org/10.1016/0016-7037\(85\)90074-2](https://doi.org/https://doi.org/10.1016/0016-7037(85)90074-2)

594 IPCC. (2023). Technical Summary. In *Climate Change 2021 – The Physical Science Basis* (pp. 35-144).
595 <https://doi.org/10.1017/9781009157896.002>

596 Iyer, G., Hultman, N., Eom, J., McJeon, H., Patel, P., & Clarke, L. (2015). Diffusion of low-carbon technologies and
597 the feasibility of long-term climate targets. *Technological Forecasting and Social Change*, 90, 103-118.
598 <https://doi.org/10.1016/j.techfore.2013.08.025>

599 Kapp, E. M. (1928). The precipitation of calcium and magnesium from sea water by sodium hydroxide. *The
600 Biological Bulletin*, 55(6), 453-458.

601 Kellock, C., Castillo Alvarez, M. C., Finch, A., Penkman, K., Kroger, R., Clog, M., & Allison, N. (2022). Optimising a
602 method for aragonite precipitation in simulated biogenic calcification media. *PLoS One*, 17(12),
603 e0278627. <https://doi.org/https://doi.org/10.1371/journal.pone.0278627>

604 Kheshti, H. S. (1995). Sequestering atmospheric carbon dioxide by increasing ocean alkalinity. *Energy*, 20(9), 915-
605 922. [https://doi.org/https://doi.org/10.1016/0360-5442\(95\)00035-F](https://doi.org/https://doi.org/10.1016/0360-5442(95)00035-F)

606 Marín-Samper, L., Arístegui, J., Hernández-Hernández, N., Ortiz, J., Archer, S. D., Ludwig, A., & Riebesell, U.
607 (2024). Assessing the impact of CO₂-equilibrated ocean alkalinity enhancement on microbial metabolic
608 rates in an oligotrophic system. *Biogeosciences*, 21(11), 2859-2876. [https://doi.org/10.5194/bg-21-
609 2859-2024](https://doi.org/10.5194/bg-21-2859-2024)

610 Marion, G., Millero, F., & Feistel, R. (2009). Precipitation of solid phase calcium carbonates and their effect on
611 application of seawater S A–T–P models. *Ocean science*, 5(3), 285-291.
612 <https://doi.org/https://doi.org/10.5194/os-5-285-2009>

613 Minx, J. C., Lamb, W. F., Callaghan, M. W., Fuss, S., Hilaire, J., Creutzig, F., Amann, T., Beringer, T., de Oliveira
614 Garcia, W., Hartmann, J., Khanna, T., Lenzi, D., Luderer, G., Nemet, G. F., Rogelj, J., Smith, P., Vicente
615 Vicente, J. L., Wilcox, J., & del Mar Zamora Dominguez, M. (2018). Negative emissions—Part 1: Research
616 landscape and synthesis. *Environmental Research Letters*, 13(6). [https://doi.org/10.1088/1748-
617 9326/aabf9b](https://doi.org/10.1088/1748-9326/aabf9b)

618 Moras, C. A., Bach, L. T., Cyronak, T., Joannes-Boyau, R., & Schulz, K. G. (2022). Ocean alkalinity enhancement –
619 avoiding runaway CaCO₃ precipitation during quick and hydrated lime dissolution. *Biogeosciences*,
620 19(15), 3537-3557. <https://doi.org/https://doi.org/10.5194/bg-19-3537-2022>

621 Moras, C. A., Cyronak, T., Bach, L. T., Joannes-Boyau, R., & Schulz, K. G. (2024). Effects of grain size and seawater
622 salinity on magnesium hydroxide dissolution and secondary calcium carbonate precipitation kinetics:
623 implications for ocean alkalinity enhancement. *Biogeosciences*, 21(14), 3463-3475.
624 <https://doi.org/10.5194/bg-21-3463-2024>

625 Morse, J. W., Arvidson, R. S., & Lüttge, A. (2007). Calcium carbonate formation and dissolution. *Chemical reviews*,
626 107(2), 342-381. <https://doi.org/https://doi.org/10.1021/cr050358j>

627 Morse, J. W., Gledhill, D. K., & Millero, F. J. (2003). CaCO₃ precipitation kinetics in waters from the great Bahama
628 bank. *Geochimica et Cosmochimica Acta*, 67(15), 2819-2826.
629 [https://doi.org/https://doi.org/10.1016/s0016-7037\(03\)00103-0](https://doi.org/https://doi.org/10.1016/s0016-7037(03)00103-0)

630 Morse, J. W., & He, S. (1993). Influences of T, S and PCO₂ on the pseudo-homogeneous precipitation of CaCO₃
631 from seawater: implications for whiting formation. *Marine Chemistry*, 41(4), 291-297.
632 [https://doi.org/https://doi.org/10.1016/0304-4203\(93\)90261-L](https://doi.org/https://doi.org/10.1016/0304-4203(93)90261-L)

633 Mucci, A., & Morse, J. W. (1983). The incorporation of Mg²⁺ and Sr²⁺ into calcite overgrowths: influences of
634 growth rate and solution composition. *Geochimica et Cosmochimica Acta*, 47(2), 217-233.
635 [https://doi.org/https://doi.org/10.1016/0016-7037\(83\)90135-7](https://doi.org/https://doi.org/10.1016/0016-7037(83)90135-7)

636 Oschlies, A., Bach, L. T., Rickaby, R. E. M., Satterfield, T., Webb, R., & Gattuso, J.-P. (2023). Climate targets, carbon
637 dioxide removal, and the potential role of ocean alkalinity enhancement. *State of the Planet, 2-oae2023*,
638 1-9. <https://doi.org/10.5194/sp-2-oae2023-1-2023>

639 Ou, Y., Xue, Z. G., & Hu, X. (2025). A numerical assessment of ocean alkalinity enhancement efficiency on a river-
640 dominated continental shelf – a case study in the northern Gulf of Mexico. *Environmental Research*
641 *Letters*. <https://doi.org/10.1088/1748-9326/adaa8b>

642 Pan, Y., Li, Y., Ma, Q., He, H., Wang, S., Sun, Z., Cai, W.-J., Dong, B., Di, Y., Fu, W., & Chen, C.-T. A. (2021). The role
643 of Mg²⁺ in inhibiting CaCO₃ precipitation from seawater. *Marine Chemistry*, 237.
644 <https://doi.org/https://doi.org/10.1016/j.marchem.2021.104036>

645 Paul, A. J., Haunost, M., Goldenberg, S. U., Hartmann, J., Sanchez, N. S., Schneider, J., Suitner, N., & Riebesell, U.
646 (2024). Ocean alkalinity enhancement in an open ocean ecosystem: Biogeochemical responses and
647 carbon storage durability. *EGUsphere*. <https://doi.org/https://doi.org/10.5194/egusphere-2024-417>

648 Pokrovsky, O. S. (1998). Precipitation of calcium and magnesium carbonates from homogeneous supersaturated
649 solutions. *Journal of Crystal Growth*, 186(1-2), 233-239. [https://doi.org/https://doi.org/10.1016/S0022-0248\(97\)00462-4](https://doi.org/https://doi.org/10.1016/S0022-0248(97)00462-4)

650 Pytkowicz, R. (1973). Calcium carbonate retention in supersaturated seawater. *American Journal of Science*,
651 273(6), 515-522. <https://doi.org/http://dx.doi.org/10.2475/ajs.273.6.515>

652 Pytkowicz, R. M. (1965). Rates of Inorganic Calcium Carbonate Nucleation. *The Journal of Geology*, 73(1), 196-
653 199. <https://doi.org/10.1086/627056>

654 Ramírez, L., Pozzo-Pirotta, L. J., Trebec, A., Manzanares-Vázquez, V., Díez, J. L., Arístegui, J., Riebesell, U., Archer,
655 S. D., & Segovia, M. (2024). Ocean Alkalinity Enhancement (OAE) does not cause cellular stress in a
656 phytoplankton community of the sub-tropical Atlantic Ocean. *EGUsphere*, 2024, 1-34.
657 <https://doi.org/https://doi.org/10.5194/egusphere-2024-847>

658 Rau, G. H., & Caldeira, K. (1999). Enhanced carbonate dissolution as a means of sequestering carbon dioxide in
659 the ocean. *Energy Conversion and Management*, 40(17), 1803-1813. [https://doi.org/10.1016/S0196-8904\(99\)00071-0](https://doi.org/10.1016/S0196-8904(99)00071-0)

660 Renforth, P., & Henderson, G. (2017). Assessing ocean alkalinity for carbon sequestration. *Reviews of Geophysics*,
661 55(3), 636-674. <https://doi.org/https://doi.org/10.1002/2016rg000533>

662 Ringham, M. C., Hirtle, N., Shaw, C., Lu, X., Herndon, J., Carter, B. R., & Eisaman, M. D. (2024). An assessment of
663 ocean alkalinity enhancement using aqueous hydroxides: kinetics, efficiency, and precipitation
664 thresholds. *Biogeosciences*, 21(15), 3551-3570. <https://doi.org/https://doi.org/10.5194/bg-21-3551-2024>

665 Rogelj, J., Popp, A., Calvin, K. V., Luderer, G., Emmerling, J., Gernaat, D., Fujimori, S., Strefler, J., Hasegawa, T.,
666 Marangoni, G., Krey, V., Kriegler, E., Riahi, K., van Vuuren, D. P., Doelman, J., Drouet, L., Edmonds, J.,
667 Fricko, O., Harmsen, M.,...Tavoni, M. (2018). Scenarios towards limiting global mean temperature
668 increase below 1.5 °C. *Nature Climate Change*, 8(4), 325-332. <https://doi.org/10.1038/s41558-018-0091-3>

669 Sánchez, N., Goldenberg, S. U., Brüggemann, D., Jaspers, C., Taucher, J., & Riebesell, U. (2024). Plankton food
670 web structure and productivity under ocean alkalinity enhancement. *Science Advances*, 10(49),
671 eado0264. <https://doi.org/doi:10.1126/sciadv.ado0264>

672 Schulz, K. G., Bach, L. T., & Dickson, A. G. (2023). Seawater carbonate chemistry considerations for ocean
673 alkalinity enhancement research: theory, measurements, and calculations. *Guide to Best Practices in*
674 *Ocean Alkalinity Enhancement Research, 2-oae2023*, 2. <https://doi.org/10.5194/sp-2-oae2023-2-2023>

675 Schwinger, J., Bourgeois, T., & Rickels, W. (2024). On the emission-path dependency of the efficiency of ocean
676 alkalinity enhancement. *Environmental Research Letters*, 19(7). <https://doi.org/10.1088/1748-9326/ad5a27>

677 Sers, M. R., & Victor, P. A. (2018). The Energy-emissions Trap. *Ecological Economics*, 151, 10-21.
678 <https://doi.org/10.1016/j.ecolecon.2018.04.004>

679 Sjöberg, E. (1976). A fundamental equation for calcite dissolution kinetics. *Geochimica et Cosmochimica Acta*,
680 40(4), 441-447. [https://doi.org/https://doi.org/10.1016/0016-7037\(76\)90009-0](https://doi.org/https://doi.org/10.1016/0016-7037(76)90009-0)

681 Söhnel, O., & Mullin, J. W. (1988). Interpretation of crystallization induction periods. *Journal of colloid and*
682 *interface science*, 123(1), 43-50. [https://doi.org/https://doi.org/10.1016/0021-9797\(88\)90219-6](https://doi.org/https://doi.org/10.1016/0021-9797(88)90219-6)

688 Suessle, P., Taucher, J., Goldenberg, S., Baumann, M., Spilling, K., Noche-Ferreira, A., Vanharanta, M., & Riebesell,
689 U. (2023). Particle fluxes by subtropical pelagic communities under ocean alkalinity enhancement.
690 *EGUsphere*, 2023, 1-26. <https://doi.org/https://doi.org/10.5194/egusphere-2023-2800>
691 Suitner, N., Faucher, G., Lim, C., Schneider, J., Moras, C. A., Riebesell, U., & Hartmann, J. (2024). Ocean alkalinity
692 enhancement approaches and the predictability of runaway precipitation processes: results of an
693 experimental study to determine critical alkalinity ranges for safe and sustainable application scenarios.
694 *Biogeosciences*, 21(20), 4587-4604. <https://doi.org/10.5194/bg-21-4587-2024>
695 Tjørve, K. M., & Tjørve, E. (2017). The use of Gompertz models in growth analyses, and new Gompertz-model
696 approach: An addition to the Unified-Richards family. *PLoS One*, 12(6), e0178691.
697 <https://doi.org/https://doi.org/10.1371/journal.pone.0178691>
698 UNFCCC. (2015). Report of the Conference of the Parties to the United Nations Framework Convention on
699 Climate Change (21st Session, 2015: Paris). Retrived December. Vol. 4. 2015.
700 Varliero, S., Buono, A., Caserini, S., Raos, G., & Macchi, P. (2024). Chemical Aspect of Ocean Liming for CO2
701 Removal: Dissolution Kinetics of Calcium Hydroxide in Seawater. *ACS Engineering Au*.
702 <https://doi.org/https://doi.org/10.1021/acsengineeringau.4c00008>
703 Wang, H., Pilcher, D. J., Kearney, K. A., Cross, J. N., Shugart, O. M., Eisaman, M. D., & Carter, B. R. (2023). Simulated
704 impact of ocean alkalinity enhancement on atmospheric CO2 removal in the Bering Sea. *Earth's Future*,
705 11(1). [https://doi.org/ https://doi.org/10.1029/2022EF002816](https://doi.org/https://doi.org/10.1029/2022EF002816)
706 Wells, M. L., & Goldberg, E. D. (1992). Marine submicron particles. *Marine Chemistry*, 40(1-2), 5-18.
707 [https://doi.org/https://doi.org/10.1016/0304-4203\(92\)90045-C](https://doi.org/https://doi.org/10.1016/0304-4203(92)90045-C)
708 Wurgaft, E., Steiner, Z., Luz, B., & Lazar, B. (2016). Evidence for inorganic precipitation of CaCO3 on suspended
709 solids in the open water of the Red Sea. *Marine Chemistry*, 186, 145-155.
710 <https://doi.org/https://doi.org/10.1016/j.marchem.2016.09.006>
711 Wurgaft, E., Wang, Z. A., Churchill, J. H., Dellapenna, T., Song, S., Du, J., Ringham, M. C., Rivlin, T., & Lazar, B.
712 (2021). Particle Triggered Reactions as an Important Mechanism of Alkalinity and Inorganic Carbon
713 Removal in River Plumes. *Geophysical Research Letters*, 48(11), 277.
714 <https://doi.org/https://doi.org/10.1029/2021gl093178>
715 Xin, X., Goldenberg, S. U., Taucher, J., Stuhr, A., Aristegui, J., & Riebesell, U. (2024). Resilience of Phytoplankton
716 and Microzooplankton Communities under Ocean Alkalinity Enhancement in the Oligotrophic Ocean.
717 *Environ Sci Technol*. <https://doi.org/10.1021/acs.est.4c09838>
718 Zeebe, R., & Wolf-Gladrow, D. (2001). *CO2 in Seawater: Equilibrium, Kinetics, Isotopes*. Elsevier Oceanography
719 Book Series. 65.
720 Zhong, S., & Mucci, A. (1989). Calcite and aragonite precipitation from seawater solutions of various salinities:
721 Precipitation rates and overgrowth compositions. *Chemical geology*, 78(3-4), 283-299.
722 [https://doi.org/https://doi.org/10.1016/0009-2541\(89\)90064-8](https://doi.org/https://doi.org/10.1016/0009-2541(89)90064-8)
723 Zhou, M., Tyka, M. D., Ho, D. T., Yankovsky, E., Bachman, S., Nicholas, T., Karspeck, A. R., & Long, M. C. (2024).
724 Mapping the global variation in the efficiency of ocean alkalinity enhancement for carbon dioxide
725 removal. *Nature Climate Change*, 1-7. <https://doi.org/https://doi.org/10.1038/s41558-024-02179-9>

726